Magnetic, transport, and thermodynamic properties of $CaMn_2O_4$ single crystals

B. D. White,[1] J. A. Souza,[1,*] C. Chiorescu,[2] J. J. Neumeier,[1,†] and J. L. Cohn[2]
[1]*Department of Physics, Montana State University, P.O. Box 173840, Bozeman, Montana 59717-3840, USA*
[2]*Department of Physics, University of Miami, Coral Gables, Florida 33124, USA*

(Received 9 December 2008; revised manuscript received 12 February 2009; published 24 March 2009)

Physical properties including magnetic susceptibility, room-temperature electrical resistivity, thermal conductivity, heat capacity, and thermal expansion are reported for high quality single-crystal samples of marokite $CaMn_2O_4$. We determined that $CaMn_2O_4$ is highly electrically insulating and exhibits long-range antiferromagnetic order below $T_N=217.5\pm0.6$ K with easy axis along *a*. Anisotropic thermal expansion, similar to that of crystallographically layered materials, is observed, suggesting that the crystal structure of $CaMn_2O_4$ is also assembled from previously undescribed layers. An extensive thermodynamic study of the antiferromagnetic transition was undertaken resulting in a heat-capacity critical exponent $\alpha=0.082\pm0.007$ and calculated pressure derivative $dT_N/dP=5.154\pm0.174$ K/GPa.

DOI: 10.1103/PhysRevB.79.104427 PACS number(s): 75.47.Lx, 75.50.Ee, 71.70.Ej, 65.40.De

I. INTRODUCTION

Initial studies of $CaMn_2O_4$ were published shortly after its discovery in 1963 in Morocco as a naturally occurring mineral.[1] It was subsequently named marokite for its country of origin and was found to crystallize in an orthorhombic structure with space group[2] *Pbcm* and exhibit antiferromagnetic (AFM) ordering below 225 K.[3] But in the decades following these preliminary investigations, further studies are completely absent in the literature until 2001, when $CaMn_2O_4$ was studied as an impurity phase in the solid-state synthesis of manganese oxides exhibiting colossal magnetoresistance behavior.[4] $CaMn_2O_4$ has since enjoyed some renewed interest; however, recently published studies have been primarily limited to reporting on aspects of the magnetic ordering[4–6] and crystal structure.[4,5,7] An extensive physical property characterization of $CaMn_2O_4$ has yet to be conducted.

Compounds with chemical formula AB_2O_4 frequently crystallize in the cubic spinel structure with space group $Fd3m$ or a tetragonally distorted spinel structure with space group $I4_1/amd$. This is true of several manganese oxide compounds: NMn$_2$O$_4$ with N=Ni, Cu, Mn, Zn, Cd, Mg, and Li.[8,9] The crystal structure of $CaMn_2O_4$ is displayed in Fig. 1 as generated by JAVA STRUCTURE VIEWER.[10] It is primarily constructed from a complex network of MnO_6 octahedra. We can formulate a convenient description of this network by considering zigzag layers of edge-sharing octahedra running parallel to *b*, which are coupled along *c* by vertex sharing of apical oxygen sites. All MnO_6 octahedra are oriented with one of two tilted orientations with respect to the *c* axis and, while all octahedra display the same tilt orientation within each layer, successive zigzag layers alternate between the two. Tunnels along *a* between the zigzag layers are occupied by Ca^{2+} ions. In stoichiometric $CaMn_2O_4$, all manganese ions are nominally high-spin Mn^{3+} ($3d^4, t_{2g}^3 e_g^1$). This electronic configuration is well known to result in highly Jahn-Teller (JT) distorted MnO_6 octahedra. Neutron-diffraction studies observe 26% elongation of the axial Mn-O bond distances relative to equatorial in the octahedra.[4] The magnitude of this distortion certainly excludes the possibility of a cubic spinel structure for $CaMn_2O_4$ but does not directly prevent the stabilization of a tetragonally distorted spinel structure. However, the large Ca^{2+} ions do inhibit tetragonal symmetry. The A site in the spinel structure is located in a position which forms AO_4 tetrahedra. Comparison of the ionic radii of all divalent ions occupying a tetrahedral site reveals that Ca^{2+} has the largest ionic radius of any with only Pb^{2+} and Hg^{2+} being slightly smaller.[11] Most other divalent ions in this situation (those generally occupying the A site of compounds which do crystallize in the spinel structure) have ionic radii 50%–70% as large as Ca^{2+} (1.00 Å).[11] The structure of $CaMn_2O_4$ is stabilized when Ca^{2+} incorporates itself into eightfold coordination with CaO_8 polyhedra instead of CaO_4 tetrahedra.[4,5] Many cubic spinel compounds exhibit a structural phase transition under pressure to one of three related orthorhombic structures—those of $CaMn_2O_4$ (*Pbcm*), $CaFe_2O_4$ (*Pnma*), and $CaTi_2O_4$ (*Cmcm*).[8] This observation

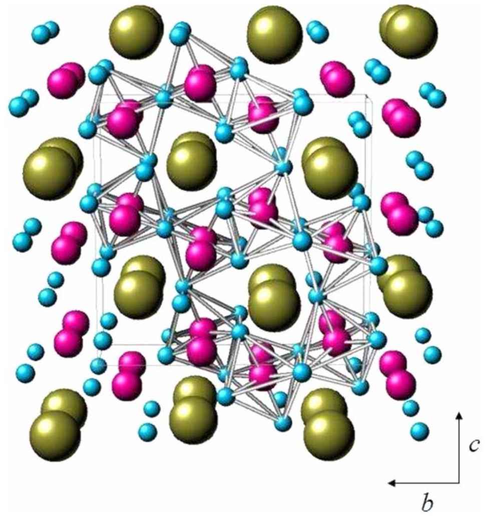

FIG. 1. (Color online) Crystal structure of $CaMn_2O_4$ viewed roughly along *a* [perspective has small *c*-axis component to visually clarify details of the three-dimensional (3D) structure]. MnO_6 octahedra are explicitly displayed within a single unit cell revealing a complex network with large Ca^{2+} ions occupying tunnels along *a* between zigzag layers built along *b*.

may imply that the chemical pressure exerted on the $CaMn_2O_4$ structure by Ca^{2+} ions is similar to the effect hydrostatic pressure has on cubic spinel compounds. It is the combination of distorted MnO_6 octahedra and large Ca^{2+} ions which results in a unique crystal structure for $CaMn_2O_4$, generally referred to as the marokite structure.[5]

$CaMn_2O_4$ is a model JT system whose structural relationship with the spinels potentially helps to bridge the divide between spinel and manganate physics. Furthermore, the textbook AFM transition exhibited by $CaMn_2O_4$ creates a unique opportunity to perform a detailed thermodynamic study of an exemplary continuous phase transition. With this in mind, we present herein measurements of magnetic susceptibility, electrical resistivity, thermal transport, heat capacity, and thermal expansion for single crystalline $CaMn_2O_4$.

II. EXPERIMENT

High quality single crystals of $CaMn_2O_4$ were grown using the standard floating zone method and characterized as described previously.[12] A representative crystal boule was oriented with back-reflection Laue diffraction, and three parallelepiped samples with millimeter dimensions were cut and polished each with longest dimension parallel to one of the three orthorhombic lattice parameters to within 1°. All measurements were performed on these oriented parallelepiped samples.

Magnetization and heat-capacity measurements were conducted with vibrating sample magnetometer (VSM) and heat-capacity options, respectively, using a physical properties measurement system (PPMS) from Quantum Design. Magnetic susceptibility measurements above 400 K were conducted with the VSM oven option in high vacuum. The heat-capacity option uses a thermal relaxation technique. The accuracy of the data depends on the sample's thermal coupling with the sample stage but can be estimated to be better than $\pm 1\%$ for temperatures between 100 and 300 K and $\pm 3-5\%$ for data below 100 K.[13] Thermal-expansion measurements were made using a capacitance dilatometer cell constructed of fused quartz.[14] The resulting data is sensitive[14] to length changes on the order of 0.1 Å. Thermal conductivity was measured in a radiation-shielded vacuum probe using a 25-μm-diameter differential chromel/constantan thermocouple and steady-state technique. Heat losses via radiation and conduction through leads were determined in separate experiments and the data were corrected accordingly. This correction was typically 10%–15% near room temperature and $\sim 2\%$ for $T \approx 150$ K. Electrical resistance was measured at room temperature using an electrometer.

III. MAGNETIC SUSCEPTIBILITY

AFM order below $T_N = 220$ K has been previously observed in both magnetization[4,5] and neutron-diffraction[3–5] studies of $CaMn_2O_4$. As the temperature is lowered through T_N, the symmetry of the magnetic superstructure was found to require a doubling of the crystallographic a axis to define the magnetic unit cell[4,5] which is described by the Γ_2 irreducible representation of the space group[5] *Pbca*. Neutron-diffraction studies of the magnetic structure observed that the AFM sublattices antialign along the a axis with negligible canting along the b and c axes.[4,5] JT distortion of the MnO_6 octahedra creates six unique Mn-O bond lengths.[4,5,7] As a result, there are six distinct superexchange interaction strengths between neighboring Mn^{3+} ions facilitated through the oxygen ions that their MnO_6 octahedra share. Whangbo *et al.*[6] studied these superexchange interactions in detail, calculating a spin exchange parameter $J = J_{AFM} + J_{FM}$ for each superexchange pathway using spin dimer analysis. They concluded with confidence that four interactions were AFM. The remaining two were observed to be weakly AFM from their calculations, though they noted that neutron-diffraction experiments[4] suggest a weakly ferromagnetic interaction is possible. The latter scenario enables the potential for weak magnetic frustration.

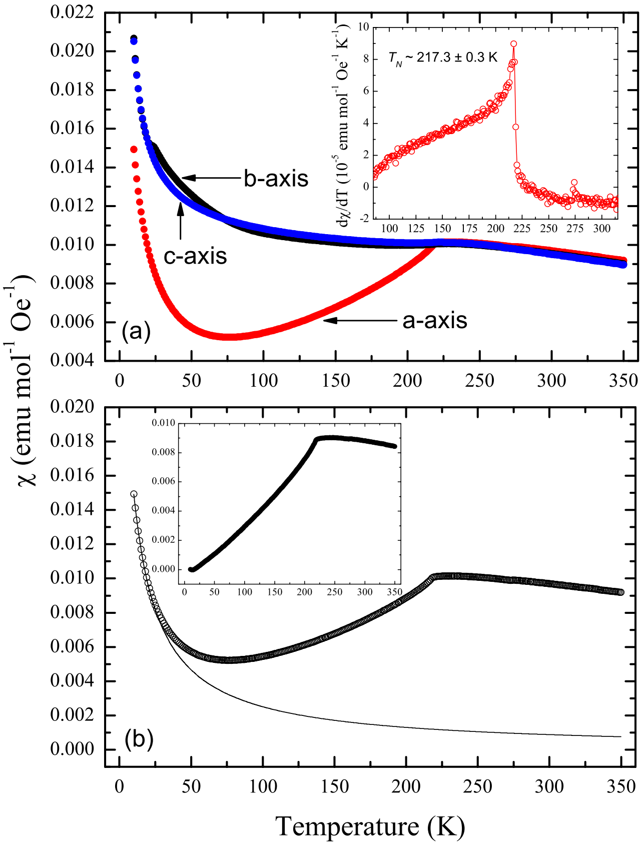

FIG. 2. (Color online) (a) Magnetic susceptibility χ measured along all three crystallographic axes in an applied field of 2000 Oe. The inset reveals the peak at T_N in $d\chi_a/dT$. (b) Curie-Weiss fit to the low-temperature upturn in χ_a (line) is plotted with χ_a (open circles). The inset displays χ_a after the low-temperature Curie-Weiss behavior is subtracted.

Magnetic susceptibility χ was measured, after zero-field cooling, between 10 and 350 K in an applied field of 2000 Oe. The results are displayed in Fig. 2(a). The behavior of χ along each axis is best described within three temperature regions. Well above T_N, $CaMn_2O_4$ is expected to exhibit paramagnetism (PM) described by the Curie-Weiss (CW) law.[4,5] AFM ordering is observed along each axis just below 220 K; however, the anomaly along a is much more distinct than along b and c (consistent with the previous identification of a as the magnetic easy axis).[4,5] The true value of T_N is somewhat difficult to extract from χ. In lieu of a better method, we identify the temperature of the peak in $d\chi/dT$ as the Néel temperature ($T_N = 217.3 \pm 0.3$ K). This is shown in the inset of Fig. 2(a). Below T_N, χ exhibits the textbook characteristics of AFM order within an anisotropic magnetic structure until ~75 K when an upturn is observed. This same upturn has been previously reported in polycrystalline samples where explanations have invoked scenarios where either spin canting[5] or a minor, Mn-based magnetic impurity phase[4,5] was responsible. Our results support the latter position as will be explained in detail.

Proper analysis of the CW behavior of $CaMn_2O_4$ requires subtraction of temperature-independent diamagnetism (DM), χ_D, and Van Vleck PM, χ_{VV}. The DM contribution, associated with filled electronic shells in the core ions, is $\chi_D = -7.610 \times 10^{-5}$ emu mol^{-1} Oe^{-1} as calculated from tabulated[15] ionic values. The Van Vleck contribution is more challenging to calculate; however, χ_{VV} is expected to be of the same order as χ_D. Conduction-electron contributions leading to Pauli PM, χ_P, can be completely neglected because of the electrically insulating behavior measured in transport properties (see Sec. IV). After non-CW contributions were subtracted from χ, we fit the data to the CW law for PM: $\chi_{CW} = C/(T - \Theta_{CW})$, where C is the Curie constant $C = (Np^2\mu_B^2)/3k_B$, $p^2 = g^2 J(J+1)$, and Θ_{CW} is the CW temperature. We assumed the Landé g factor is 2.0 and that the orbital angular momentum is quenched by the oxygen crystal field[4,5] so that $J = S$. CW fits below 400 K result in unreasonable values for S (expected to be 2.0 given the Mn^{3+} high-spin electronic state), which are inconsistent with the chemical characterization of our samples.[12] Magnetic susceptibility (not shown) was subsequently measured for a randomly oriented sample between 300 and 500 K to fit at higher temperature. It is evident that above 420 K, deviations from CW behavior, likely due to short-range magnetic order, become insignificant. Between 420 and 500 K, the fit is optimized by $C = 6.896 \pm 0.005$ emu K mol^{-1} Oe^{-1} and $\Theta_{CW} = -376.8 \pm 0.6$ K. If we assume there are exactly two Mn ions per $CaMn_2O_4$ unit (good to within about 1%),[12] then each contributes an average spin of $S = 2.174$ which is about 9% higher than expected. The most plausible explanation for this is that there is an additional contribution to χ which must be subtracted to isolate CW behavior. The negative value of Θ_{CW} is consistent with long-range AFM order.

The upturn in χ below 75 K in Fig. 2(a) is reminiscent of PM. It appears to be isotropic which should probably disqualify spin canting as a possible explanation. Assuming this is correct, χ below T_N, after accounting for χ_D and χ_{VV}, is composed of contributions associated with an AFM ordering χ_{AFM} and a simple PM background χ_{CW}. $CaMn_2O_4$ displays typical χ_{AFM} behavior wherein χ approaches zero along a (easy axis) and is weakly temperature dependent (almost constant) along b and c. Though we cannot reliably subtract χ_{AFM} from χ, we can fit the upturn with the CW law between 10 and 17 K where χ_{AFM} is roughly zero along a and approximately constant along b and c. The fit along the a-axis upturn can be seen in Fig. 2(b). CW fits to the upturns provide values for Θ_{CW}: 8.17, 12.10, and 13.56 K along a, b, and c, respectively. We consider only Θ_{CW} here because we derived a relationship between the Θ_{CW} values, optimized along different directions i and j, by assuming $\chi = \chi_{CW} + \chi_{AFM}$.

$$\Theta_{CW,i} = \frac{C_j' - C_i'}{\chi_{AFM}^i} + T\left(1 - \frac{\chi_{AFM}^j}{\chi_{AFM}^i}\right) + \Theta_{CW,j}\frac{\chi_{AFM}^j}{\chi_{AFM}^i}. \quad (1)$$

In Eq. (1), C_i' is the Curie constant extracted from data which includes the contribution from χ_{AFM}^i. If the underlying nature of the upturn in $CaMn_2O_4$ is truly PM, the CW fits to them should provide Θ_{CW} values related by Eq. (1). In the special case where $\chi_{AFM}^i \approx \chi_{AFM}^j$, as is true along b and c [see Fig. 2(a)], Eq. (1) simplifies to

$$\Theta_{CW,i} = \frac{C_j' - C_i'}{\chi_{AFM}^i} + \Theta_{CW,j}. \quad (2)$$

Using Eq. (2), we estimate that the difference between $\Theta_{CW,b}$ and $\Theta_{CW,c}$ should be approximately 2.95 K; the actual difference is found to be 1.5 K. The discrepancy is surely related to our assumption that the AFM susceptibility contributions along b and c are identical.

After establishing the nature of the upturn as probably PM, the next step is to identify which ions are responsible. We expect a negligibly low level of impurities to exist in the samples themselves as was demonstrated by several chemical characterization methods.[12] Therefore, the PM ions are necessarily identified as manganese ions. Oxygen nonstoichiometry in the samples leads directly to the formation of small amounts of Mn^{4+} or Mn^{2+} depending on whether excess oxygen has been absorbed or the samples are oxygen deficient, respectively. Measurements of the average manganese valence in crystals using iodometric titration have shown that an average of ~1% of all manganese ions was in the Mn^{4+} oxidation state.[12] The most accurate estimate of the true Curie constant associated with the PM upturn (without the influence of χ_{AFM}) comes from the a-axis data where χ_{AFM} is the smallest. Yet, $C_a' = 0.27122$ emu K mol^{-1} Oe^{-1} implies that 7% of manganese ions would have to be Mn^{4+}, which is inconsistent with our titration results. Of course, iodometric titration is not sensitive to the difference between a Mn^{3+}-Mn^{3+} pair and a Mn^{4+}-Mn^{2+} pair. Hundley and Neumeier[16] previously suggested that accounting for charge disproportionation in $La_{1-x}Ca_xMnO_3$ ($2Mn^{3+} \rightarrow Mn^{2+} + Mn^{4+}$) is necessary to explain its temperature-dependent thermoelectric power. They claimed that in the $x = 0$ case (all Mn^{3+}), 70%–80% of all Mn^{3+} disproportionates by the time the sample is heated to 1000–1300 K. Only 4% of Mn^{3+} ions would need to disproportionate (and be quenched in that state at low temperature) to result in the PM upturn we observe in $CaMn_2O_4$. More likely, however, is that samples become oxygen deficient over time as a function of annealing or conducting measurements at temperatures exceeding 300 K, and eventually Mn^{2+} sites evolve. Only 3% of manganese ions being in the Mn^{2+} state would account for the PM upturn at low temperature.

IV. TRANSPORT PROPERTIES

A. Electrical transport

The room-temperature electrical resistivity (RTR) of $CaMn_2O_4$, as measured by an electrometer along two axes, reveals insulating behavior: $\rho_a = 2.70 \times 10^8\ \Omega$ cm and $\rho_c = 2.14 \times 10^8\ \Omega$ cm. Repeated measurements along the b axis were unsuccessful, with RTR values in excess of $10^{12}\ \Omega$; though it is believed that this is related to contact resistance problems rather than anisotropy. In order to better understand these results without the aid of band-structure calculations or spectroscopy measurements, we compare them with RTR values for related materials. We are able to immediately contrast $CaMn_2O_4$ with the other ternary calcium manganese oxides $CaMnO_3$, Ca_2MnO_4, $Ca_3Mn_2O_7$, and $Ca_4Mn_3O_{10}$, which belong to a Ruddlesden-Popper series of structurally related phases. Their RTR values are 12.3, 1.1×10^4, 1.3×10^3, and $8.32 \times 10^2\ \Omega$ cm, respectively, as determined with polycrystalline samples,[17] though measurements of single crystalline $CaMnO_3$ yield slightly lower RTR on the order of $1\ \Omega$ cm.[18] Insulating layers of CaO planes isolate the connectivity of MnO_6 octahedra along c in Ca_2MnO_4, $Ca_3Mn_2O_7$, and $Ca_4Mn_3O_{10}$, accounting for their relatively large RTR. However, high RTR values in $CaMn_2O_4$ cannot be ascribed to insulating CaO planes and no MnO_6 octahedra are isolated in its crystal structure (see Fig. 1). The crystal structure of $CaMnO_3$ also contains no insulating CaO planes, enjoying instead an unbroken, simple octahedral network along all three crystallographic axes. This explains its predictably lower resistivity when compared with Ca_2MnO_4, $Ca_3Mn_2O_7$, and $Ca_4Mn_3O_{10}$.

The definitive distinction between $CaMn_2O_4$ and other calcium manganese oxide phases is that it is composed entirely of Mn^{3+} ions rather than Mn^{4+}, which results in highly JT distorted MnO_6 octahedra. It is therefore more instructional to consider the behaviors of other compounds containing JT distorted octahedra. The most well-studied material fitting this description is $LaMnO_3$, generally considered to be a Mott insulator with RTR between 10^3 and $10^5\ \Omega$ cm depending on Refs. 19 and 20 (highly sensitive to oxygen nonstoichiometry). Studies of $LaMnO_3$ in the vicinity of the JT transition at T_{JT} have demonstrated a significant resistivity decrease above T_{JT} when the distortion of the MnO_6 octahedra is relieved.[19–21] In fact, optical conductivity measurements[22] reveal the opening of a gap below T_{JT} in the electronic structure of $LaMnO_3$—a gap whose existence is predicted by band-structure calculations.[23] The onset of JT distortion lifts the degeneracy of the e_g levels opening a gap between the half-filled $d_{3z^2-r^2}$ and empty $d_{x^2-y^2}$ orbitals. It seems reasonable that an energy gap originating from the JT distortion could also be responsible for insulating behavior in $CaMn_2O_4$. The magnitude of distortion in $CaMn_2O_4$ is much larger than in $LaMnO_3$ according to neutron refinements[4,24] at 300 K (26% versus 10% increase in elongated bond lengths versus equatorial bonds). Insulating behavior is also observed in $MgMn_2O_4$ with RTR value of $4 \times 10^5\ \Omega$ cm.[25] $MgMn_2O_4$ is quite similar to $CaMn_2O_4$ in that JT distortion forces its crystal structure to deviate from the ideal cubic spinel structure to lower symmetry (in this case a tetragonal structure). Though there are more, these two examples indicate a probable correlation between JT distortion and an electrically insulating ground state. If the size of the band gap scales at all with the magnitude of distortion, the high RTR values of $CaMn_2O_4$ are completely consistent with that picture.

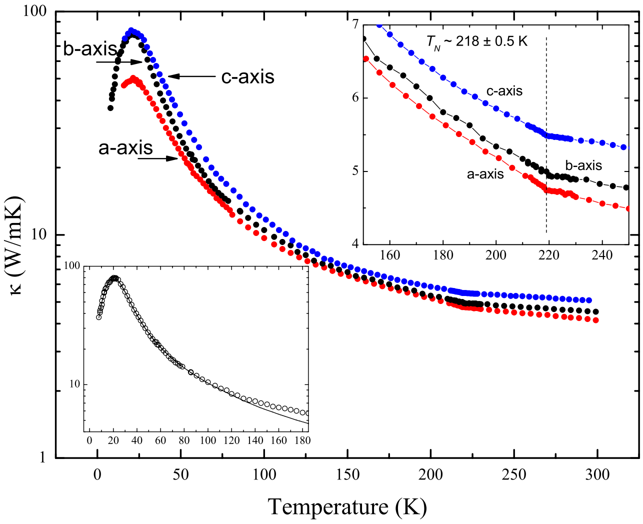

FIG. 3. (Color online) Thermal conductivity κ measured along all three crystallographic axes. The upper inset shows an anomaly in κ at T_N resulting from magnetostrictive effects that modify the phonon dispersion (lines are a guide to the eyes). The lower inset displays low-temperature fits (solid line through data) to κ using the Debye-Calloway model.

Finally, we can conclude that the high RTR values are reflective of the high quality of the single-crystal samples. Even relatively low levels of impurities or defects would manifest themselves as impurity conduction—a scenario which is not observed.

B. Thermal transport

The thermal conductivity κ for all three transport directions is shown in Fig. 3. The sharp maxima near 20 K are typical signatures of lattice conduction in crystalline insulators having modest imperfections. Any spin-wave contribution is likely negligible in comparison to that of the lattice except at the very lowest temperatures (<1 K). The Debye-Calloway model[26] was found to provide an excellent description of the data for $T \leq 125$ K (see the lower inset of Fig. 3). A sum of relaxation rates representing phonon scattering by other phonons (Umklapp processes), sheetlike faults, and pointlike defects was employed with forms, $A_1\omega^2 T e^{(-\Theta_D/4T)}$, $A_2\omega^2$, and $A_3\omega^4$, respectively ($\omega = vq$ is the phonon frequency). A sound velocity $v = 2800$ m/s ($\Theta_D = 384$ K) provided the best fit to κ for all orientations, indicating isotropic elastic properties. Parameter values in the ranges $A_1 = (1.8-2.1) \times 10^{-17}$ s/K, $A_2 = (1.6-2.1) \times 10^{-17}$ s, and $A_3 = (3-8) \times 10^{-44}$ s^3 were employed for the b- and c-axis data; defect terms (A_2 and A_3) two to four times larger were required to model the a-axis data. Whether this difference can be attributed to the magnetism or is simply a consequence of a higher defect concentration in the a-axis specimen will

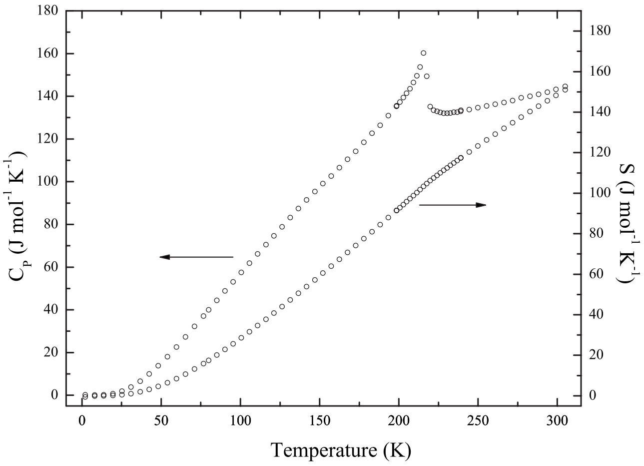

FIG. 4. Heat capacity at constant pressure (left abscissa) and entropy (right abscissa).

require further measurements to determine. AFM domain boundaries are a likely source of strain that can scatter heat-carrying acoustic phonons, and it is possible that such scattering is enhanced for heat flow along the magnetic easy axis. The phonon mean-free paths at 10 K, inferred from the values of κ and the specific heat (see Sec. V) $\ell = 3\kappa / C_P \approx 10-20\ \mu$m, are for all specimens substantially smaller than the minimum crystal dimension (0.5–0.7 mm). This indicates, consistent with the model fitting, that boundary scattering was negligible.

At higher temperatures, the slope-change anomalies in κ at T_N (see upper inset of Fig. 3) are typical of magnetostrictive effects that modify the phonon dispersion and/or scattering. The slope change occurs at $T_N = 218 \pm 0.5$ K, in rough agreement with the result from magnetization ($T_N = 217.3 \pm 0.3$ K). The temperature dependence of κ in the PM phase is considerably weaker than the $\kappa \sim 1/T^n$ ($n \sim 1-2$) behavior typical of anharmonic decay. Similarly weak temperature dependencies of κ are found in the PM phases of AFM materials such as MnO,[27] $CaMnO_3$,[28,29] and $YMnO_3$ (Ref. 30) and have been attributed to phonon scattering by nanoscale strain generated by spin fluctuations.

V. THERMODYNAMIC PROPERTIES

There are three basic thermodynamic response functions: heat capacity, compressibility, and coefficient of thermal expansion.[31] To characterize the thermodynamic nature of $CaMn_2O_4$, we measured both heat capacity and thermal expansion. Each provides critical insight individually, but simultaneous analysis using the method of Souza *et al.*[32] can also be used to extract a critical exponent α associated with the singularity at T_N and can provide a calculation for dT_N/dP.

A. Heat capacity

Heat capacity at constant pressure between 2 and 300 K is displayed in Fig. 4. A λ-peak singularity is clearly revealed at $T_N = 217.39 \pm 0.06$ K. At low temperature, we fit the data with a function of the form $C_P = \gamma T + (\beta_{\text{latt}} + \beta_{\text{AFM}}) T^3$. Terms of other orders including T^{-2}, T^2, and T^5 characterizing contributions from the nuclear moment of ^{55}Mn, long-wavelength spin-wave excitations, and higher-order lattice terms, respectively,[33] were neglected because they did not improve the fit. The linear term accounts for the electronic contribution and is characterized by the Sommerfeld parameter γ, while the cubic term describes contributions from the lattice and AFM spin excitations[33] and is characterized by $\beta_{\text{Tot}} = \beta_{\text{latt}} + \beta_{\text{AFM}}$. The fit was carried out by plotting C_P/T against T^2 and by fitting a linear region below 42 K. It was optimized with $\gamma = 0$ J mol^{-1} K^{-2} (a negligible value is not surprising in light of the insulating behavior discussed in Sec. IV) and $\beta_{\text{Tot}} = 1.367 \times 10^{-4}$ J mol^{-1} K^{-4}. The Debye temperature was estimated to be $\Theta_D = 463 \pm 4$ K. However, Θ_D, is proportional to $\beta_{\text{latt}}^{-1/3}$, and because there is no method to decouple β_{latt} from β_{Tot}, we expect our estimate to be slightly lower than the true value.

The heat capacity was measured to highest temperature at 305 K at which it is about 145 J mol^{-1} K^{-1} and continues to trend upward as shown in Fig. 4. At still higher temperature, it should asymptotically approach $21R \approx 174.6$ J mol^{-1} K^{-1} as predicted by the classical law of Dulong-Petit for a crystal with seven atoms per formula unit, though the asymptotic value may be smaller due to the contribution of lighter oxygen atoms.[34] Classically, it should asymptotically approach $21R$ well above Θ_D, so our high-temperature data appear to be entirely consistent with expected behavior.

The molar entropy, S, was calculated by $\int [C_P/T] dT$ while constraining the integration constant so that $S \to 0$ as $T \to 0$. It is displayed in Fig. 4 with C_P. The total molar entropy change from 2 to 305 K was 151.5 ± 0.5 J mol^{-1} K^{-1}. The magnetic entropy contribution S_{Mag} associated with the transition can be extracted from the calculated entropy by subtracting from S an entropy background (representing all nonmagnetic contributions), calculated with a polynomial fit of S between 80–305 K excluding the region immediately around the singularity.[32] The change in entropy due to AFM spin ordering was found to be $\Delta S_{\text{Mag}} = 1.19 \pm 0.03$ J mol^{-1} K^{-1}. We can compare this with the somewhat naïve calculation of N spins per mole, randomly oriented with $S_{\text{Mag}} = 2R \ln 2$, which transition to a perfectly ordered state with $S_{\text{Mag}} = 0 (\Delta S_{\text{Mag}} = 11.53$ J mol^{-1} K^{-1}). The large disparity between experiment and model is attributed to unintentional inclusion of magnetic entropy contributions to the subtracted entropy background. The observation of magnetic fluctuations leading to departure from CW behavior up to 200 K above T_N suggests short-range order exists well above the temperature range we considered when extracting S_{Mag}. Furthermore, deviation from Debye behavior above 120 K suggests a significant continuation of AFM ordering well below T_N. These observations indicate the necessity of expanding the temperature range far beyond the vicinity of the singularity to properly extract S_{Mag} (we constrained S_{Mag} to the boundaries of the singularity). This task is inhibited by the nontrivial difficulty of reliably subtracting other entropy contributions in those regions where the magnetic contribution is by no means obvious.

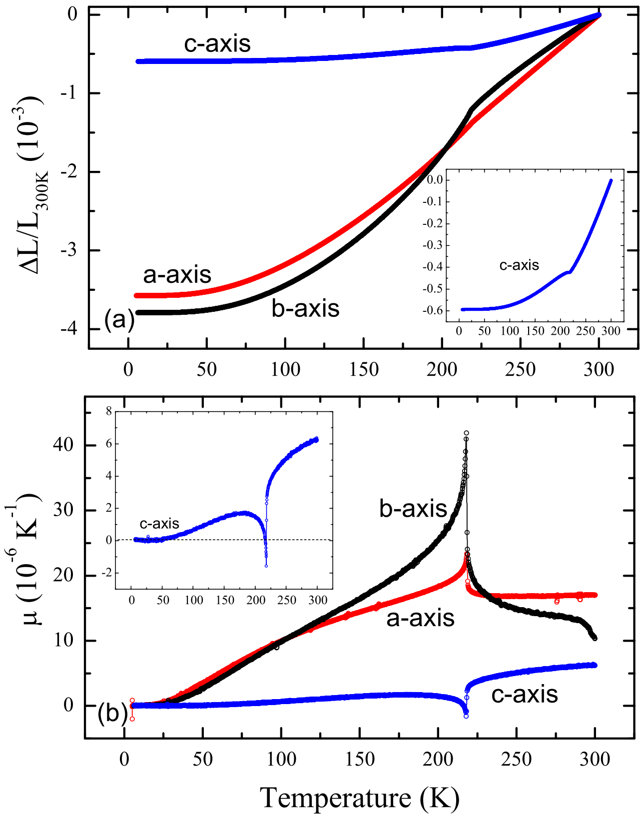

FIG. 5. (Color online) (a) Linear thermal expansion $\Delta L/L$ along all three crystallographic axes. The inset displays $\Delta L/L$ along the c axis in better detail to reveal the striking nature of the anomaly at T_N. (b) The coefficients of linear thermal expansion $\mu = d(\Delta L/L)/dT$ are displayed together to highlight the λ peak in each direction at T_N. The inset displays the coefficient along the c axis with the dotted line running along zero to highlight the two temperature ranges where thermal expansion is negative.

B. Thermal expansion

Linear thermal expansion $\Delta L/L$, normalized at 295 K, is plotted in Fig. 5(a), revealing anisotropic behavior comparable to compounds with layered crystal structures such as Na_xCoO_2 and $YBa_2Cu_3O_{7-\delta}$ wherein a strong anisotropy exists between inter- and intralayer $\Delta L/L$.[35,36] The transition at T_N is clearly visible as kinks in $\Delta L/L$, most pronounced along b and c. All three axes contract with decreasing temperature throughout the measured temperature range except along c, where an expansion takes place just below T_N and again below 25 K before contracting at 8 K. The inset of Fig. 5(a) highlights the complex detail of $\Delta L/L$ along the c axis. Negative thermal expansion at low temperature may be associated with thermal population of anomalous phonon modes[37] and is common in layered systems. Comparison reveals that the behavior along a and b (interlayer) is qualitatively similar with a few subtle differences. Above 200 K, the a axis experiences the largest relative contraction of the three crystallographic axes, but the onset of magnetic order at T_N results in a higher rate of contraction with decreasing temperature along b, while modifying the contraction rate along a comparatively little. This contraction rate disparity below T_N results in more relative contraction along b than a below 200 K. The c-axis contraction is much smaller than the other two axes. A similar anisotropy is often observed in layered materials, suggesting that the "layers" in the a-b plane might share similar phonon-dispersion characteristics. However, the quasi-two-dimensional (2D) nature of the crystal structure does not result in 2D magnetic behavior because superexchange calculations suggest that the interlayer coupling between MnO_6 zigzag chains is as strong as the intralayer coupling.[6] Refinements of lattice parameters from powder neutron-diffraction report relative reductions of 0.38%, 0.43%, and 0.060% between 300 and 20 K for Δa, Δb, and Δc, respectively.[4] Our direct measurements of $\Delta L/L$ provide consistent results in the same temperature range: 0.358%, 0.379%, and 0.059% for Δa, Δb, and Δc, respectively. The slight difference should be attributed to a combination of uncertainty in the neutron-diffraction refinements and a minor admixture of contributions from the c axis in our measurements along a and b, the result of which reduces the total relative contraction along those axes.

The linear coefficient of thermal expansion $\mu = d(\Delta L/L)/dT$ is a more thermodynamically relevant quantity than $\Delta L/L$. Results for μ (point by point derivatives of our $\Delta L/L$ data with no fitting or smoothing) are displayed in Fig. 5(b). There are three general features that require some attention. First, the λ-shape singularities at T_N are clearly indicative of the continuous nature of the phase transition. AFM ordering at T_N results in strains along a and b opposite in direction to the strain along c. Similar opposing strains[35,36] are observed at T_N in Na_xCoO_2 and T_c in $YBa_2Cu_3O_{7-\delta}$. We defer our full analysis of the features in C_P and $\Omega = \mu_a + \mu_b + \mu_c$ to Sec. VI where a simultaneous analysis is conducted. Second, μ along each axis asymptotically approaches zero as temperature approaches zero. This is required by the third law of thermodynamics given the definition: $\mu L \equiv -(\partial S/\partial P)_T$. Finally, μ increases rapidly with increasing temperature around 25 K. This is especially apparent along a and b. C_P increases at the same temperature (see Fig. 4), suggesting that this behavior designates the onset of strong phonon activity. Consequently, we observe the anharmonic peak in κ (displayed in Fig. 3) at about the same temperature.

C. Analysis of paramagnetic-antiferromagnetic phase transition

Deep insight into the nature of a magnetic phase transition is gained from careful analysis of its critical behavior. The singularity in heat capacity around T_c originates from a nonanalytic term in the thermodynamic free energy and can be asymptotically described by a function of the form

$$C_P^* = \left(\frac{A_\pm}{\alpha_\pm}\right)|t|^{-\alpha_\pm} + B_\pm + Dt, \qquad (3)$$

where t is the reduced temperature $t \equiv (T - T_c)/T_c$; $A_\pm$, $B_\pm$, and D are constants; and $\alpha_\pm$ is the critical exponent.[32,38] Quantities with plus-minus subscripts denote[39] values above (+) and below (−) T_c. Equation (3) describes a simple power-law divergence in $|t|$, completely characterized by the critical exponents $\alpha_\pm$, with a simple linear background. $\alpha_\pm$ could be positive or negative, though it is clear from Eq. (3) that these

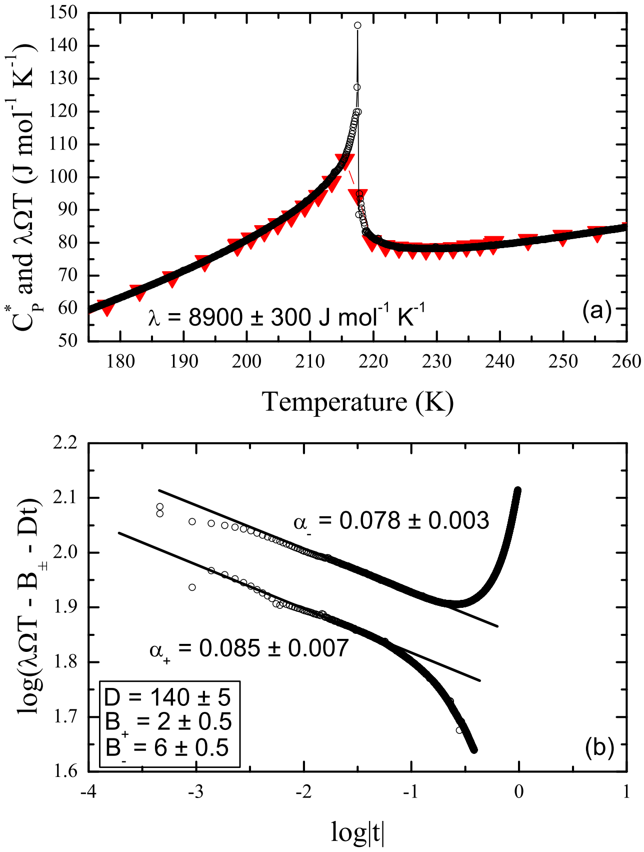

FIG. 6. (Color online) (a) Overlap between C_P^* (triangles) and $\lambda T\Omega$ (open circles) in the critical temperature region around T_N. (b) Critical behavior above and below T_N as characterized by linear fits of thermal-expansion data on a log-log plot.

two scenarios lead to drastically different physical results: C_P^* diverges at T_c for $\alpha_\pm > 0$ while it remains finite at T_c for $\alpha_\pm < 0$ ($C_P^* = B$ where $B_+ = B_- = B$). Once determined, the value of $\alpha_\pm$ can be compared with predictions from a variety of universality classes or related materials.

Extracting $\alpha_\pm$ from heat-capacity data is nontrivial because the data density required is not practical with the thermal relaxation technique. Also, the inability to warm a sample uniformly and simultaneously leads to a smaller effective sample size and averaging effects which are especially detrimental in the vicinity of the sharp singularity. This results in broadening or rounding as well as a tendency to cut the singularity's peak off significantly. However, Souza *et al.*[32] demonstrated that ΩT scales with the same critical exponent as C_P^*. This is fortunate because our thermal-expansion measurements are less susceptible to the averaging effects which alter the singularity in C_P^*. After superimposing $C_P^* \equiv C_P - a - bT$ with $\lambda \Omega T$, $\alpha_\pm$ may be extracted from $\lambda \Omega T$ instead.[32] The linear term subtracted from C_P represents the lattice contribution near T_c, and λ is a constant which depends on the molar volume v and $\partial T_c / \partial P$.[32]

The overlap between C_P^* and $\lambda \Omega T$ for $CaMn_2O_4$ is optimized by $\lambda = 8900 \pm 300$ J mol^{-1} K^{-1}. As can be seen in Fig. 6(a), the quality of the overlap is excellent—a requirement for continuous phase transitions.[32] One benefit of this overlap technique[32] is that the pressure derivative of T_c may be expressed as $dT_c/dP = v/\lambda$. The molar volume of $CaMn_2O_4$ at 218 K was calculated as $v = 4.587 \pm 0.007 \times 10^{-5}$ m^3/mol using our results for $\Delta V/V = (\Delta L/L)_a + (\Delta L/L)_b + (\Delta L/L)_c$ and lattice parameters measured[4] at 300 K. This results in a pressure derivative $dT_N/dP = 5.154 \pm 0.1740$ K/GPa, but we are currently unable to compare this calculation with any direct measurement. The only published study of $CaMn_2O_4$ under pressure investigated a pressure-induced structural phase transition at 35 GPa but did not consider the AFM transition.[8] However, previous use of this technique[32,35,38] has demonstrated its reliability in other materials.

Equation (3) describes the critical behavior exhibited by C_P^*, but it is an equally valid description of the singularity in $\lambda \Omega T$. To extract $\alpha_\pm$ from the latter data set, we plotted $\log(\lambda \Omega T - B_\pm - Dt)$ and $\log(-\lambda \Omega T + B_\pm + Dt)$, suitable for $\alpha_\pm > 0$ and $\alpha_\pm < 0$, respectively, against $\log(|t|)$. Values for $B_\pm$, D, and T_N were systematically varied and refined in each case until the linear fittable range was optimized above and below T_N with the additional constraint that $\alpha_+ = \alpha_-$ within experimental uncertainty. We were unable to obtain a suitable result for any values of $B_\pm$, D, or T_N when we assumed $\alpha_\pm < 0$ (finite singularity). Assumption of a divergent transition with $\alpha_\pm > 0$ yielded significantly better results. They are displayed in Fig. 6(b) for $D = 140 \pm 5$ J mol^{-1} K^{-1}, $B_+ = 2 \pm 0.5$ J mol^{-1} K^{-1}, $B_- = 6 \pm 0.5$ J mol^{-1} K^{-1}, and $T_N = 217.5 \pm 0.1$ K. These parameters result in critical exponents $\alpha_+ = 0.085 \pm 0.007$ and $\alpha_- = 0.078 \pm 0.003$. The critical region is larger below T_N, as can be observed in Fig. 6(b), though not significantly. A similar observation has been made in other materials[32,38] and justified by assuming that the prefactors for the correlation length, which also exhibits critical behavior $\xi \sim g_\pm |t|^{-\nu}$ with exponent ν, obey $g_+ < g_-$.

The critical exponent associated with the AFM transition in $CaMn_2O_4$ is 0.082 ± 0.007, calculated by averaging α_+ and α_-. However, this value cannot be positively assigned to any currently existing universality class. Unfortunately, the vast majority of critical exponent calculations has concentrated solely on ferromagnetics. For a typical AFM universality class, too many fixed points exist within the renormalization-group perspective, making calculations extremely cumbersome, and few Monte Carlo studies[40] currently exist. It has been suggested that for simple AFM order on a loose-packed lattice the ferromagnetic predictions for corresponding universality classes are equivalent.[41] But this could only include a few elementary AFM materials, among which $CaMn_2O_4$ cannot be counted. We are, however, able to compare this exponent with experimental results for MnF_2 ($0 < \alpha < 0.1$) (Ref. 42) and contrast it with Co_3O_4 (-0.15 ± 0.06) (Ref. 43) and NiO (-0.118 ± 0.006).[44] Further work, both theoretical and experimental, is required on materials with similar magnetic behavior to say anything definitive about this exponent, beyond that it is consistent with our identification of a continuous magnetic phase transition.

VI. CONCLUSION

Physical properties including magnetic susceptibility, room-temperature electrical resistivity, thermal conductivity, heat capacity, and thermal expansion are reported for single-crystal CaMn$_2$O$_4$. We determined that CaMn$_2$O$_4$ is highly electrically insulating from measurements of resistance at room temperature. Identification of an insulating ground state is consistent with the Sommerfeld parameter extracted from heat capacity and the anharmonic peak observed in thermal conductivity. Comparison with LaMnO$_3$ and other manganese oxides composed of Mn^{3+}, and therefore JT distorted MnO$_6$ octahedra, seems to demonstrate a correlation between JT distortion and insulating behavior. The high degree of JT distortion in CaMn$_2$O$_4$ is expected to be responsible for these observations. Magnetic susceptibility measurements are consistent with long-range AFM order below $T_N = 217.5 \pm 0.6$ K with easy axis along a. T_N is reported from considering the anomalies in all our measurements (except electrical resistivity) and is several degrees below the temperature previously stated in neutron and magnetization studies.[4,5] An isotropic upturn in magnetic susceptibility along all three crystallographic axes is determined to be a paramagnetic contribution from non-Mn^{3+} manganese ions which exist in small amounts due to oxygen nonstoichiometry. Thermal-expansion measurements suggest that CaMn$_2$O$_4$ may be considered layered from a crystallographic perspective as it exhibits the same anisotropy observed in layered compounds. These layers may be identified as the zigzag chains of edge-sharing MnO$_6$ octahedra running parallel to b with edge-sharing connectivity along a and vertex sharing of every other octahedron along c. The effect of this structure is to provide a quasi-2D nature to the phonons, while magnetic superexchange interactions[6] remain relatively isotropic and 3D in nature. An extensive thermodynamic study of the AFM transition was undertaken using simultaneous analysis of heat capacity and thermal-expansion coefficient[32] resulting in a heat-capacity critical exponent $\alpha = 0.082 \pm 0.007$ and calculated pressure derivative $dT_N/dP = 5.154 \pm 0.174$ K/GPa. We are currently unable to conclude anything definitive about our value of α except that it is consistent with a continuous phase transition.

ACKNOWLEDGMENTS

This material is based on work supported by the National Science Foundation (Grants No. DMR-0504769 and No. DMR-0072276), the U.S. Department of Energy, Office of Basic Energy Sciences (Contract No. DE-FG-06ER46269), the Brazilian agency CNPq (Grant No. 201017/2005-9), and the Research Corporation. Helpful discussions with R. K. Bollinger, M. S. da Luz, and Y.-K. Yu are gratefully acknowledged.

---

[*] Permanent address: Centro de Ciências Naturais e Humanas, Universidade Federal do ABC, 09090-900, Santo André, São Paulo, Brazil.

[†] Corresponding Author: neumeier@physics.montana.edu

[1] C. Gaudefroy, G. Jouravsky, and F. Permingeat, Bull. Soc. Fr. Mineral. Cristallogr. **86**, 359 (1963).

[2] M. M. Couffon, G. Rocher, and J. Protas, Acad. Sci., Paris, C. R. **258**, 1847 (1964).

[3] Y. Allain and B. Boucher, J. Phys. (Paris) **26**, 789 (1965).

[4] C. D. Ling, J. J. Neumeier, and D. N. Argyriou, J. Solid State Chem. **160**, 167 (2001).

[5] S. Zouari, L. Ranno, A. Cheikh-Rouhou, O. Isnard, M. Pernet, P. Wolfers, and P. Strobel, J. Alloys Compd. **353**, 5 (2003).

[6] M.-H. Whangbo, H.-J. Koo, D. Dai, and D. Jung, Inorg. Chem. **41**, 5575 (2002).

[7] H. G. Giesber, W. T. Pennington, and J. W. Kolis, Acta Crystallogr., Sect. C: Cryst. Struct. Commun. **57**, 329 (2001).

[8] Z. Wang, S. K. Saxena, and J. J. Neumeier, J. Solid State Chem. **170**, 382 (2003).

[9] L. Malavasi, C. Tealdi, G. Flor, and M. Amboage, Phys. Rev. B **71**, 174102 (2005).

[10] S. Weber, J. Appl. Crystallogr. **32**, 1027 (1999).

[11] R. D. Shannon, Acta Crystallogr. A **32**, 751 (1976).

[12] B. D. White, C. A. M. dos Santos, J. A. Souza, K. J. McClellan, and J. J. Neumeier, J. Cryst. Growth **310**, 3325 (2008).

[13] J. C. Lashley, M. F. Hundley, A. Migliori, J. L. Sarrao, P. G. Pagliuso, T. W. Darling, M. Jaime, J. C. Cooley, W. L. Hults, L. Morales, D. J. Thoma, J. L. Smith, J. Boerio-Goates, B. F. Woodfield, G. R. Stewart, R. A. Fisher, and N. E. Phillips, Cryogenics **43**, 369 (2003).

[14] J. J. Neumeier, R. K. Bollinger, G. E. Timmins, C. R. Lane, R. D. Krogstad, and J. Macaluso, Rev. Sci. Instrum. **79**, 033903 (2008).

[15] Landolt-Bornstein, in *New Series, Group II*, edited by K.-H. Hellwege and A. M. Hellwege (Springer-Verlag, Heidelberg, 1986), Vol. 16.

[16] M. F. Hundley and J. J. Neumeier, Phys. Rev. B **55**, 11511 (1997).

[17] I. D. Fawcett, J. E. Sunstrom IV, M. Greenblatt, M. Croft, and K. V. Ramanujachary, Chem. Mater. **10**, 3643 (1998).

[18] J. L. Cohn, C. Chiorescu, and J. J. Neumeier, Phys. Rev. B **72**, 024422 (2005).

[19] J.-S. Zhou and J. B. Goodenough, Phys. Rev. B **60**, R15002 (1999).

[20] P. Mandal, B. Bandyopadhyay, and B. Ghosh, Phys. Rev. B **64**, 180405(R) (2001).

[21] J. A. Souza, J. J. Neumeier, R. K. Bollinger, B. McGuire, C. A. M. dos Santos, and H. Terashita, Phys. Rev. B **76**, 024407 (2007).

[22] K. Tobe, T. Kimura, Y. Okimoto, and Y. Tokura, Phys. Rev. B **64**, 184421 (2001).

[23] D. V. Efremov and D. I. Khomskii, Phys. Rev. B **72**, 012402 (2005).

[24] P. Norby, I. G. Krogh Andersen, and E. Krogh Andersen, J. Solid State Chem. **119**, 191 (1995).

[25] H. V. Keer, M. G. Bodas, A. Bhaduri, and A. B. Biswas, J. Phys. D **7**, 2058 (1974).

[26] R. Berman, *Thermal Conduction in Solids* (Clarendon, Oxford, 1976).

[27] G. A. Slack and R. Newman, Phys. Rev. Lett. **1**, 359 (1958).

[28] J.-S. Zhou and J. B. Goodenough, Phys. Rev. B **66**, 052401 (2002).

[29] J. L. Cohn and J. J. Neumeier, Phys. Rev. B **66**, 100404(R) (2002); C. Chiorescu, J. J. Neumeier, and J. L. Cohn, Phys. Rev. Lett. **101**, 257202 (2008).

[30] P. A. Sharma, J. S. Ahn, N. Hur, S. Park, Sung Baek Kim, Seongsu Lee, J.-G. Park, S. Guha, and S.-W. Cheong, Phys. Rev. Lett. **93**, 177202 (2004).

[31] H. E. Stanley, *Introduction to Phase Transitions and Critical Phenomena* (Oxford University Press, New York, 1971).

[32] J. A. Souza, Y.-K. Yu, J. J. Neumeier, H. Terashita, and R. F. Jardim, Phys. Rev. Lett. **94**, 207209 (2005).

[33] A. L. Cornelius, B. E. Light, and J. J. Neumeier, Phys. Rev. B **68**, 014403 (2003).

[34] J. J. Neumeier and H. Terashita, Phys. Rev. B **70**, 214435 (2004).

[35] C. A. M. dos Santos, J. J. Neumeier, Y.-K. Yu, R. K. Bollinger, R. Jin, D. Mandrus, and B. C. Sales, Phys. Rev. B **74**, 132402 (2006).

[36] C. Meingast, O. Krauf, T. Wolf, H. Wühl, A. Erb, and G. Müller-Vogt, Phys. Rev. Lett. **67**, 1634 (1991).

[37] J. J. Neumeier, T. Tomita, M. Debessai, J. S. Schilling, P. W. Barnes, D. G. Hinks, and J. D. Jorgensen, Phys. Rev. B **72**, 220505(R) (2005).

[38] J. A. Souza, J. J. Neumeier, B. D. White, H. Terashita, R. F. Jardim, and Y.-K. Yu (unpublished).

[39] It is generally accepted that $\alpha_- = \alpha_+$ and, in the special case of $\alpha_\pm < 0$, $B_\pm$ is also constrained to be equal above and below T_c.

[40] H. Kawamura, J. Phys.: Condens. Matter **10**, 4707 (1998).

[41] R. G. Bowers and M. E. Woolf, Phys. Rev. **177**, 917 (1969).

[42] D. T. Teaney, Phys. Rev. Lett. **14**, 898 (1965).

[43] L. M. Khriplovich, E. V. Kholopov, and I. E. Paukov, J. Chem. Thermodyn. **14**, 207 (1982).

[44] M. Massot, A. Oleaga, A. Salazar, D. Prabhakaran, M. Martin, P. Berthet, and G. Dhalenne, Phys. Rev. B **77**, 134438 (2008).